VI International Conference on Particle-based Methods – Fundamentals and Applications
PARTICLES 2019
E. Oñate, M. Bischoff, D.R.J. Owen P. Wriggers, , & T. Zohdi (Eds)

DEM POWDER SPREADING AND SPH POWDER MELTING MODELS FOR ADDITIVE MANUFACTURING PROCESS SIMULATIONS

CLAAS BIERWISCH

Fraunhofer IWM
Wöhlerstr. 11, 79108 Freiburg, Germany
e-mail: claas.bierwisch@iwm.fraunhofer.de, www.simpartix.com

Key words: Additive manufacturing, laser-powder bed fusion, surface tension, Marangoni currents, DEM, SPH.

Abstract. Particle-based numerical methods enable different process simulations for powder bed additive manufacturing. Two examples are the simulation of powder spreading and the simulation of melting and re-solidification. From these simulations, several material properties can be extracted such as packing density after spreading, porosity and surface properties after re-solidification and, ultimately, indicators for the strength of the component. In this work simulations of powder spreading using the Discrete Element Method (DEM) as well as simulations of the melt pool dynamics by means of Smoothed Particle Hydrodynamics (SPH) are presented. Surface tension material properties are varied and the influence on the resulting surface shape is discussed. The occurrence of different surface roughness patterns can be addressed to certain dimensionless numbers, namely the Capillary number, the Marangoni number and the ratio of the laser scan speed to a characteristic Marangoni current surface velocity.

1 INTRODUCTION

Simulations of the powder spreading process were reported by Parteli et al. [1]. They carried out DEM simulations of the application of a new layer of powder with a counter-rotating roller. The grain shape is modelled by a multi-sphere approach. The key finding of this work is an increase of the roughness of the surface with the square of the translation speed of the roller. Interestingly, a powder without fines shows less roughness.

Continuum mechanical modeling studies of the melting and re-solidification process, which take into account the heat input by the laser, the heat transfer and the phase transformation of the bulk material, were carried out using the finite element method (FEM) as well as the lattice Boltzmann method (LBM). The studies can be distinguished based on whether the powder was considered explicitly as individual particles or in a homogenized bulk representation. A brief survey is given below.

1.1 Homogenized models without explicit representation of the powder

Gusarov et al. present a model describing laser absorption and heat transport for laser powder bed fusion (L-PBF) in combination with the thermodynamics during melting and re-solidification [2]. The occurrence of so-called balling, i.e., the formation of spherical

structures in the melt pool, was described in this model by a Plateau-Rayleigh instability which can be avoided by low scanning speeds. Hodge et al. present a thermomechanical continuum model for the L-PBF process [3]. They demonstrate that the energy input in a new layer leads to renewed heating and associated expansions in deeper layers. Riedlbauer et al. use FEM simulations and experiments to study the electron beam melting (EBM) process [4]. They find very good agreement for the dependencies of melt pool lifetime on line energy and on scan speed as well as of melt pool width on scan speed.

1.2 Models with explicit representation of the powder

Körner et al. describe the simulation of the energy absorption, the heat transfer and the melting and re-solidification of a powder bed in 2D using the LBM, taking into account the size distribution of the particles [5]. A key result of this work is that the powder volume fraction has a strong influence on the homogeneity of the melt pool. A high volume fraction supports the formation of a well-defined half-circle shaped pool while for a low volume fraction the pool geometry becomes sensitive to the local powder arrangement. Furthermore, the authors could derive a process diagram relating the melt track appearance to the parameters beam power and scan speed based on simulations and complementary experiments. This work was continued in Körner et al. [6] and Bauereiß et al. [7] by simulating the subsequent melting and re-solidification of several layers. The particles of a new layer are applied by a trickling algorithm rather than by a powder spreading process simulation. A key message of these works is that the stochastic properties of the powder bed in combination with wetting and capillary effects have a strong influence on defect formation during the building process.

Gürtler et al. developed a 3D continuum mechanical model for the L-PBF process [8]. By means of the volume of fluid approach, individual particles of the powder bed were represented. In comparison with experiments, basic phenomena such as porosity formation under unfavorable process conditions could be reproduced. Khairallah et al. also use a FEM continuum mechanical description of the L-PBF process in 3D [9]. By using free surfaces, individual particles in the powder bed and their distribution could be modeled. Furthermore, irregular solidification patterns could be predicted by the model. In a subsequent study, Khairallah et al. include a temperature-dependent surface tension which causes Marangoni currents as well as recoil pressure during vaporization [10]. This model allows for analyses of the complex dynamics of the melt pool with emphasis on pore formation mechanisms.

2 NUMERICAL METHODS

DEM simulations are used to study the powder spreading process. The powder particles are modeled as spheres with a finite size distribution. The particles interact through Hertzian repulsion, viscous damping, cohesion, sliding friction and rolling friction. Details of the simulation method are given in [11].

The main focus of this study is melt pool dynamics which is simulated using the SPH method. To do so, the continuity equation,

$$\frac{D\rho}{Dt} = -\rho\, \boldsymbol{\nabla} \cdot \boldsymbol{u}\,, \tag{1}$$

as well as the Navier-Stokes momentum equation,

$$\rho \frac{D\boldsymbol{u}}{Dt} = -\boldsymbol{\nabla} p + \mu \, \boldsymbol{\nabla}^2 \boldsymbol{u} + \boldsymbol{f}_\Sigma + \rho \, \boldsymbol{g} \,, \tag{2}$$

are solved. Here, $\boldsymbol{u}$ is the velocity, ρ is the mass density, p is the hydrostatic pressure, μ is the dynamic viscosity, $\boldsymbol{f}_\Sigma$ is the volumetric surface tension force and $\boldsymbol{g}$ is the acceleration due to gravity. Bold face symbols denote vector quantities.

The hydrostatic pressure is given by an equation of state,

$$p = \frac{\rho_0 \, s^2}{\gamma} \left[\left(\frac{\rho}{\rho_0} \right)^\gamma - 1 \right], \tag{3}$$

where ρ_0 is the equilibrium density, s is the speed of sound and γ is the isentropic exponent.

The melt rheology is modeled by means of a temperature-dependent viscosity. The viscosity changes depending on the state of matter of the material. Here, we differentiate three states: fully solid (S) below the solidus temperature T_S, fully liquid (L) above the liquidus temperature T_L and an intermediate state in between,

$$\mu(T) = \begin{cases} \mu_L \,, & T \geq T_L \,, \\ \mu_S + (\mu_L - \mu_S) \dfrac{T - T_S}{T_L - T_S} \,, & T_S < T < T_L \,, \\ \infty \,, & T \leq T_S \,. \end{cases} \tag{4}$$

The surface tension force,

$$\boldsymbol{f}_\Sigma = (-\sigma_N \, \kappa \, \boldsymbol{n} + \sigma_T \, \boldsymbol{\nabla}_\Sigma T) \, \delta_\Sigma \,, \tag{5}$$

is composed of a contribution normal to and a contribution tangential to the local surface. Here, σ_N is the surface tension, κ the surface curvature and $\boldsymbol{n}$ the surface unit normal vector. σ_T is the Marangoni coefficient describing the variation of surface tension with temperature and $\boldsymbol{\nabla}_\Sigma T$ is the gradient of the surface temperature field. δ_Σ is a delta function marking the location of the surface in space. Details of the SPH surface tension model are given in [12].

The balance equation for the thermal energy per unit mass e,

$$\rho \frac{De}{Dt} = k \, \boldsymbol{\nabla}^2 T - \varepsilon \, \sigma_B (T^4 - T_0^4) \, \delta_\Sigma + \frac{dI}{dz} \tag{6}$$

is composed of contributions from heat conduction, Stefan-Boltzmann radiation and absorbed laser energy. Here, k is the thermal conductivity, ε is the emissivity, σ_B is the Stefan-Boltzmann constant, T_0 is the ambient temperature and I is the local intensity of the laser radiation.

The absorption of the laser radiation along the vertical coordinate z is described by the Lambert-Beer law with an attenuation coefficient a,

$$\frac{dI}{dz} = a \, I \,. \tag{7}$$

The relation between temperature T and thermal energy per unit mass e is given by the following expression which takes into account the specific heat capacity c and the latent heat of melting H,

$$T(e) = \begin{cases} T_L + \dfrac{e - e_L}{c}\,, & e \geq e_L\,, \\ T_S + \dfrac{e - e_S}{c + \dfrac{H}{T_L - T_S}}\,, & e_S < e < e_L\,, \\ \dfrac{e}{c}\,, & e \leq e_S\,. \end{cases} \tag{8}$$

Here, $e_S = c\,T_S$ is the solidus thermal energy per unit mass and $e_L = c\,T_L + H$ is the liquidus thermal energy per unit mass.

The laser radiation is described by a Gaussian intensity profile in 2D,

$$I(x) = \frac{P}{\sqrt{2\pi}\,6\,w^2} \exp\left[-\frac{(x - x_0)^2}{2w^2}\right], \tag{9}$$

or in 3D,

$$I(x, y) = \frac{P}{2\pi\,w^2} \exp\left[-\frac{(x - x_0)^2 + (y - y_0)^2}{2w^2}\right], \tag{10}$$

with the power P, the characteristic width w and the laser spot center coordinates x_0 and y_0.

3 RESULTS

The systems simulated in this study are represented by the capillary number,

$$\mathrm{Ca} = \frac{\mu\,u}{\sigma_N}, \tag{11}$$

which describes the ratio of viscosity and surface tension and the Marangoni number,

$$\mathrm{Ma} = -\frac{\sigma_T\,\Delta T\,l\,\rho_0\,c}{\mu\,k}, \tag{12}$$

which quantifies the strength of the thermal convection at the surface. Here, u is a characteristic fluid velocity in the melt pool, l is a characteristic melt pool diameter and ΔT is a characteristic temperature difference along the melt pool.

3.1 Two-dimensional simulations

First, we study the two-dimensional simulation of a simple lattice of three layers of powder particles which is traversed by a laser producing heat. Selected snapshots of the temperature field are shown in Figure 1 for three test cases: No surface tension, surface tension and Marangoni convection. In the case without surface tension (left column), a largely homogenous surface sets after re-solidification, which still reveals the positions of the original powder particles. With surface tension (middle column), the surface is better smoothed. On the other hand, Marangoni convection currents at the surface caused by a temperature-dependent surface tension (right column) lead to a very irregular surface, which is significantly rougher than the original particle distribution.

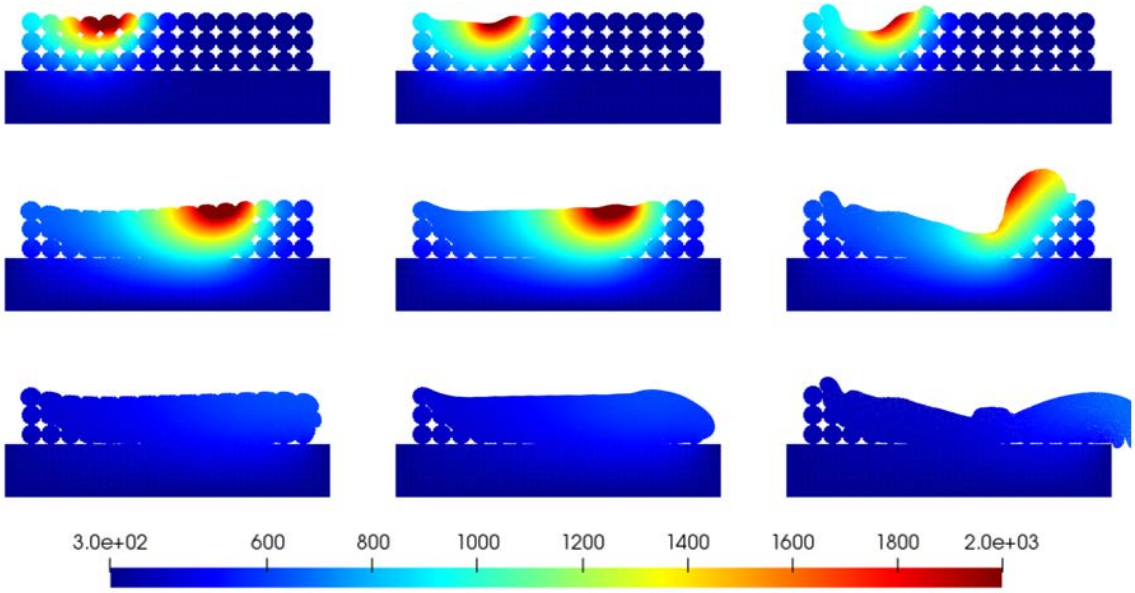

Figure 1: 2D SPH simulation of melting and re-solidification. The laser moves to the right at constant speed. The temperature field in Kelvin is color-coded. The rows represent different points in time. Left column: without surface tension (Ca = ∞, Ma = 0); middle column: with surface tension (Ca = 1, Ma = 0); right column: with Marangoni currents (Ca = 1, Ma = 150).

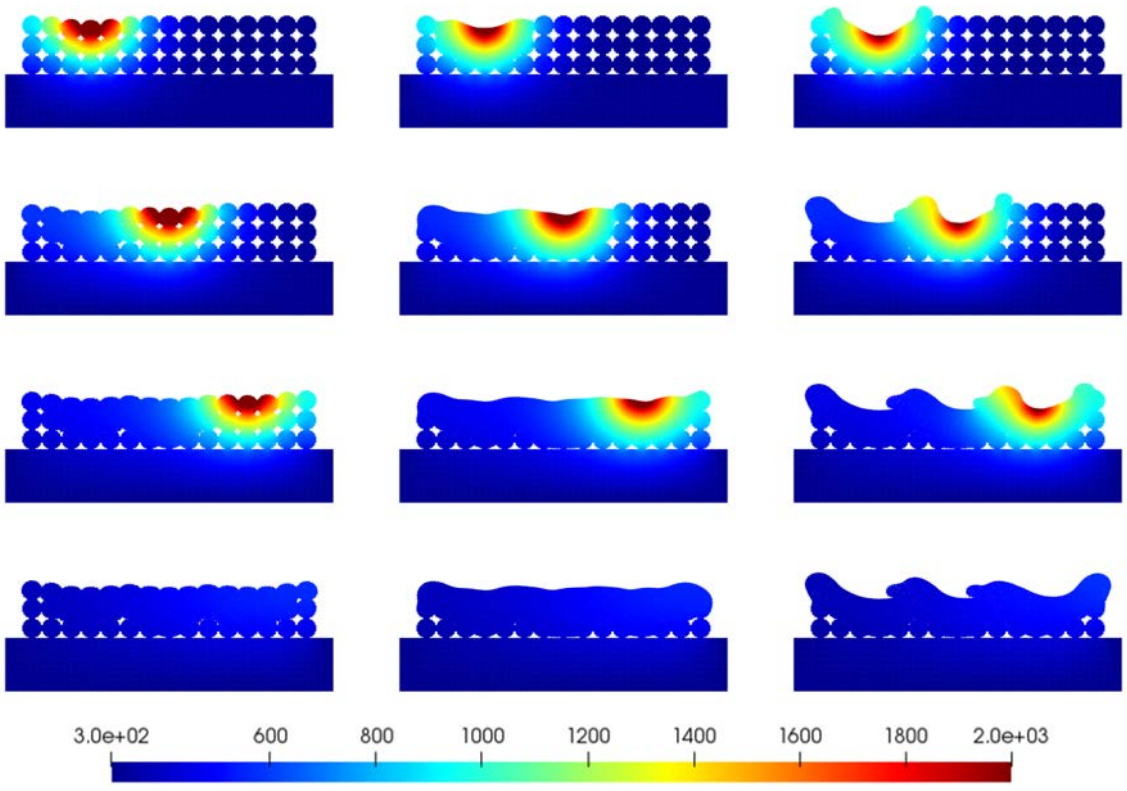

Figure 2: Like Figure 1, however, the laser remains for a certain time at one position and then changes to the next position. As a result, laser tracks into the plane of observation are approximated.

Complementary to the previous situation, laser motion into the plane of observation is now simulated. For this purpose, the position of the laser source remains constant for a certain time in the 2D simulation and then changes abruptly. The results are summarized in Figure 2. Again, in the case without surface tension (left), the initial arrangement of the powder particles is still easily recognizable. The surface tension leads to a smoothing of the surface, while still a slight ripple with a wavelength which corresponds approximately to the distance of the laser positions remains (middle). The Marangoni currents lead again to the most irregular surface (right).

3.2 Three-dimensional simulations

To create a realistic spatial powder arrangement prior to melting, a DEM simulation is performed in which a new powder layer is applied by spreading with a counter-rotating roller moving at a constant speed (see Figure 3). A section of the powder bed is then prepared using a finer spatial discretization for the following melt pool simulation (see Figure 4).

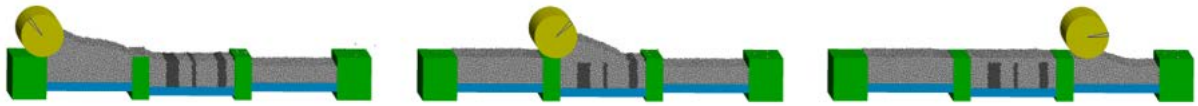

Figure 3: 3D DEM simulation of the spreading process with a counter-rotating roller.

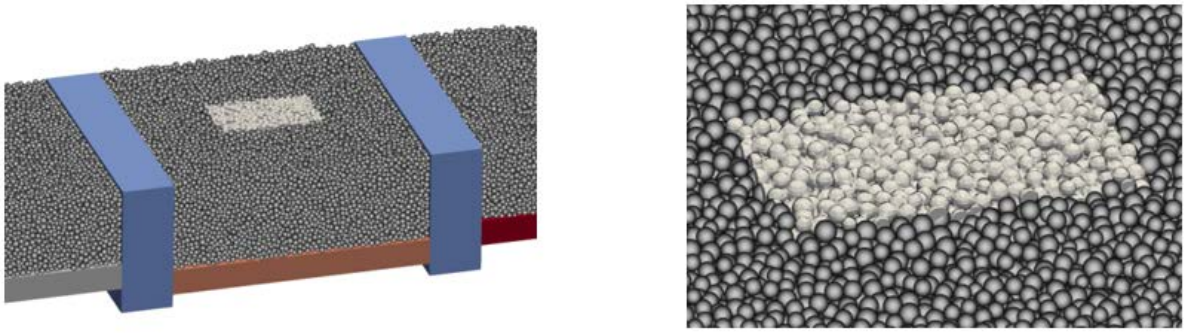

Figure 4: Particle distribution after the spreading simulation in two magnifications.
Shown in light gray is the region used for the following melt pool simulation.

Three-dimensional simulations of melting and re-solidification are again performed using the SPH method. The laser beam traverses three adjacent tracks. Figure 5 summarizes the results. For all parameter variations, the powder particles are melted along the laser tracks. Differences can be found in the occurring maximum temperatures. Without surface tension (left), the temperature is highest, while it is lowest in the case of temperature-dependent surface tension (right). This observation can be explained by the fact that without surface tension the convective heat transport is the lowest and the introduced heat is almost only removed by conduction and radiation. Surface tension enhances convective transport and Marangoni currents maximize it.

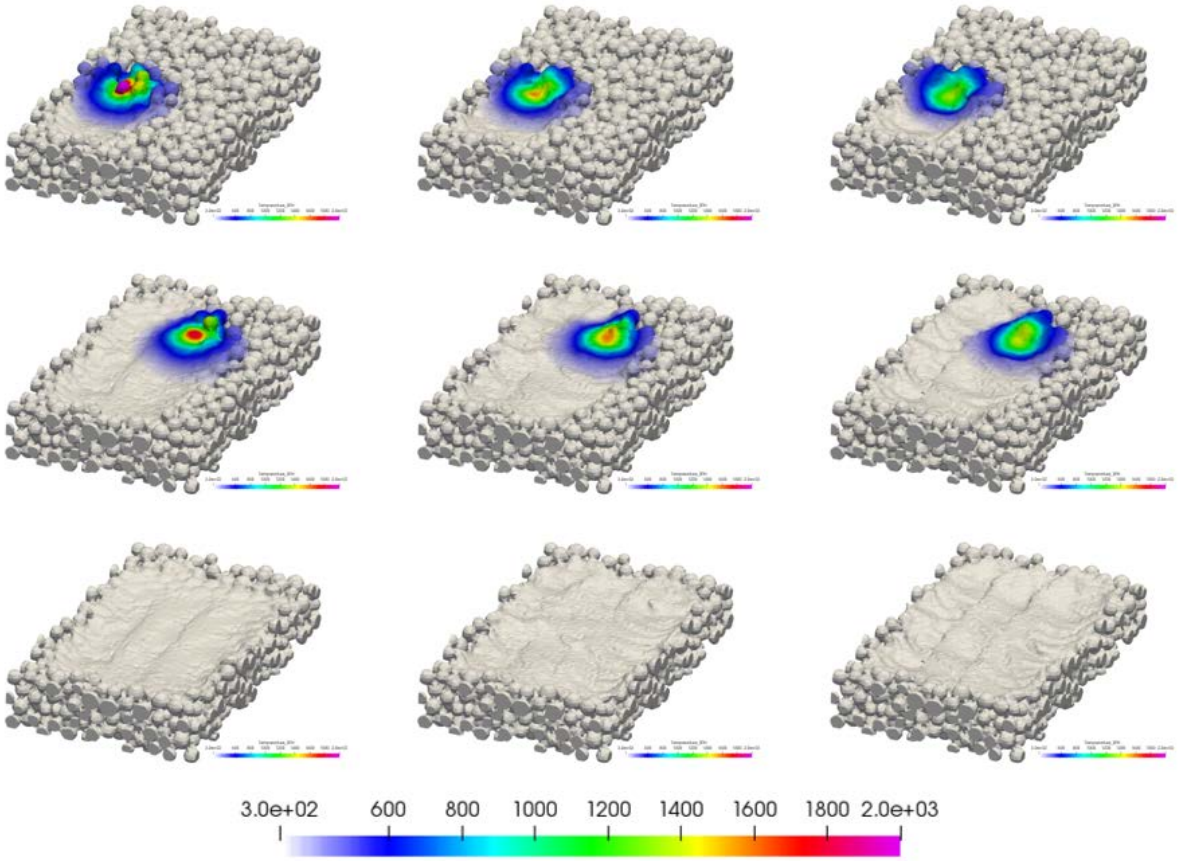

Figure 5: 3D SPH simulation of the melting and re-solidification of the arrangement of particles from the spreading simulation. The laser moves at constant speed along three equidistant tracks. The temperature field in Kelvin is color-coded. The rows represent different points in time. Left column: without surface tension ($\mathrm{Ca} = \infty, \mathrm{Ma} = 0$); middle column: with surface tension ($\mathrm{Ca} = 0.1, \mathrm{Ma} = 0$); right column: with Marangoni currents ($\mathrm{Ca} = 0.1, \mathrm{Ma} = 15$).

To analyze the resulting surface after re-solidification, Figure 6 shows the corresponding color-coded height profiles. In all profiles, the laser tracks are still visible. In the case without surface tension (left), the profile has the greatest depression approximately at the end of the first third of each track. With surface tension (center), additional scale-like structuring occurs along the laser tracks. These scale structures are most pronounced in the case of the Marangoni currents (right). Also, the height differences in the profile are the largest in that case.

The Marangoni currents in the case of a temperature-dependent surface tension are further studied by means of the surface velocity profiles in the melt pool. Figure 7 shows the velocity components along and perpendicular to the laser scan direction in addition to the height profile. For better visibility of each scan track the hatch spacing between the tracks in increased compared to the simulations shown before and, thus, only two tracks are included in the simulation.

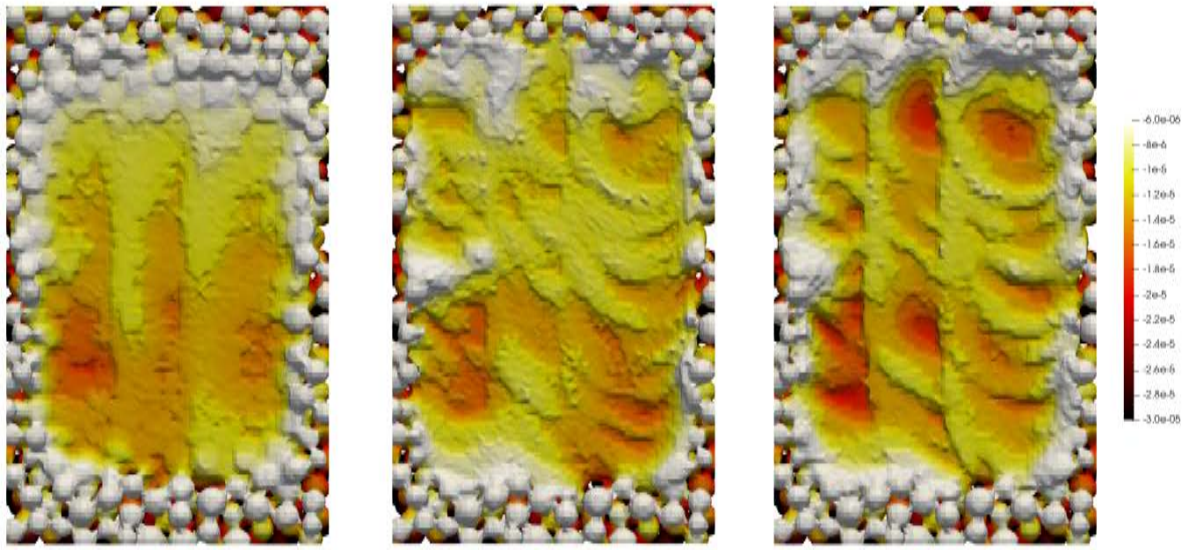

Figure 6: Color-coded height profiles in meters (red: bottom, white: top) of the simulations from Figure 5.

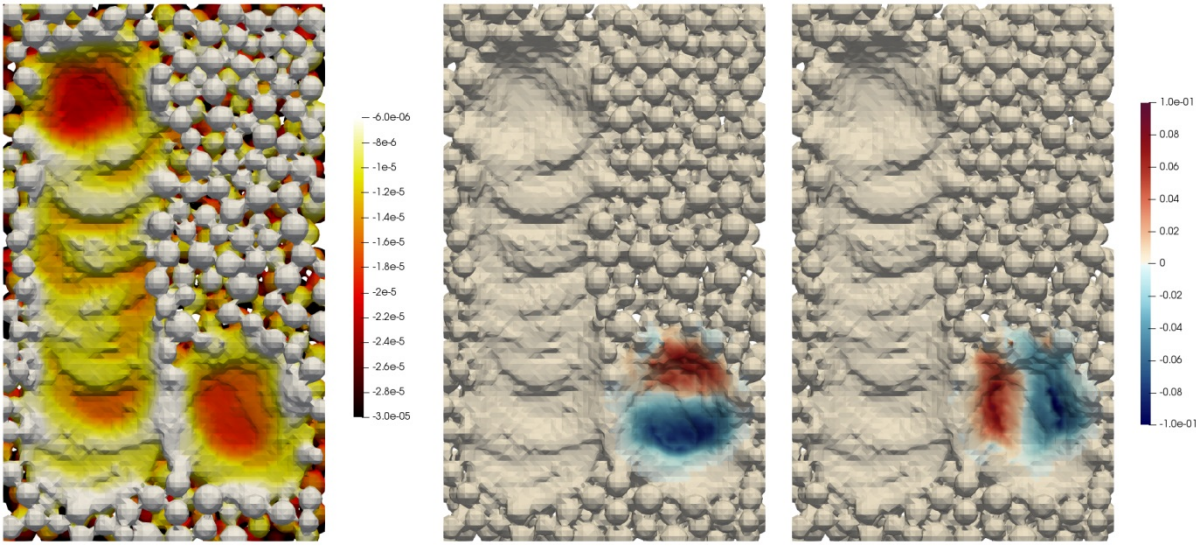

Figure 7: Height profile (left) and velocity components parallel (middle) and perpendicular (right) to the laser scan track during a simulation with a ratio of laser scan speed to Marangoni current surface velocity of 1.

It is found in both 2D and 3D simulations that the maximum Marangoni current surface velocity in the melt pool can be expressed as

$$u_S \approx -\frac{\sigma_T \, \Delta T}{20 \, \mu}. \tag{13}$$

In order to investigate the formation of the scale structures in more detail further simulations with variations of the laser scan speed c_L are carried out. In particular, the ratio of the scan speed and the surface velocity of the Marangoni current in the melt pool is analyzed. Figure 8 shows simulated height profiles using velocity ratios c_L/u_S between 1 and 10. In the case of a velocity ratio of 1 the scale pattern is clearly pronounced and rather regular. For a ratio of 3 the pattern in still discernible but less pronounced. For a ratio of 10 the scale pattern does not appear any more. This observation hints that an upper bound for the laser scan speed above which scale patterns do not occur can be expressed as

$$c_{L,\max} \approx -\frac{\sigma_T \, \Delta T}{2 \, \mu}. \tag{14}$$

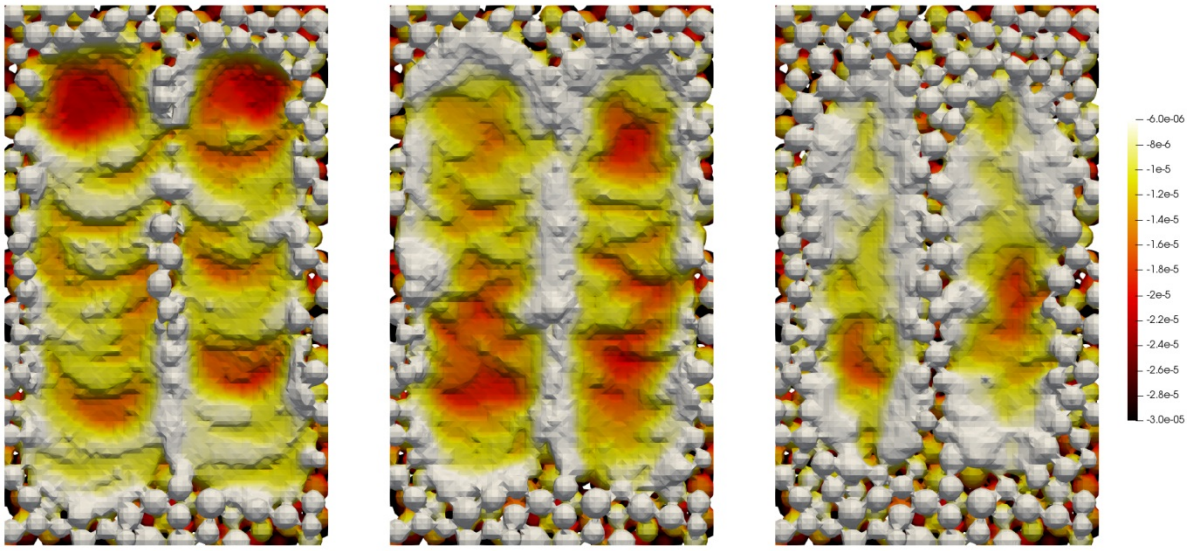

Figure 8: Color-coded height profiles of simulations with different ratios of laser scan speed to Marangoni current surface velocity. Left: $c_L/u_S \approx 1$; middle: $c_L/u_S \approx 3$; right: $c_L/u_S \approx 10$.

4 CONCLUSIONS

Particle-based simulations provide detailed insights into melt pool dynamics and are particularly suitable for the systematic investigation of the influence of process and material parameters on the process result. In this work, relations between surface tension effects and the resulting surface profile in 2D and 3D simulations are investigated as examples. It is shown that, on the one hand, surface tension can have a smoothing effect. On the other hand, especially Marangoni currents can cause a pronounced surface roughness. Dimensionless numbers allow for characterization of the emerging surface profiles based on material properties and process parameters.

5 ACKNOWLEDGEMENTS

Financial support by the Deutsche Forschungsgemeinschaft (DFG) under grant number BI 1859/2-1 within the priority program 2122 *Materials for Additive Manufacturing* is greatly acknowledged. All simulations are carried out using the SimPARTIX® software developed by Fraunhofer IWM [13].

REFERENCES

[1] Parteli, E.J.R. and Pöschel, T. Particle-based simulation of powder application in additive manufacturing. *Powder Technol.* (2016) **288**:96–102.

[2] Gusarov, A.V., Yadroitsev, I., Bertrand, Ph. and Smurov, I. Heat transfer modelling and stability analysis of selective laser melting. *Appl. Surf. Sci.* (2007) **254**(4):975–979.

[3] Hodge, N.E., Ferencz, R.M. and Solberg, J.M. Implementation of a thermomechanical model for the simulation of selective laser melting. *Comput. Mech.* (2014) **54**(1):33–51.

[4] Riedlbauer, D., Scharowsky, T., Singer, R.F., Steinmann, P., Körner, C. and Mergheim, J. Macroscopic simulation and experimental measurement of melt pool characteristics in selective electron beam melting of Ti-6Al-4V. *Int. J. Adv. Manuf. Technol.* (2017) **88**:1309–1317.

[5] Körner, C., Attar, E. and Heinl, P. Mesoscopic simulation of selective beam melting processes. *J. Mater. Process. Technol.* (2011) **211**(6): 978–987.

[6] Körner, C., Bauereiß, A. and Attar, E. Fundamental consolidation mechanisms during selective beam melting of powders. *Modelling Simul. Mater. Sci. Eng.* (2013) **21**(8):085011.

[7] Bauereiß, A., Scharowsky, T. and Körner, C. Defect generation and propagation mechanism during additive manufacturing by selective beam melting. *J. Mater. Process. Technol.* (2014) **214**(11):2522–2528.

[8] Gürtler F.-J., Karg. M., Leitz, K.-H. and Schmidt, M. Simulation of laser beam melting of steel powders using the three-dimensional volume of fluid method. *Physics Procedia* (2013) **41**:881–886.

[9] Khairallah, S.A. and Anderson, A. Mesoscopic simulation model of selective laser melting of stainless steel powder. *J. Mater. Process. Technol.* (2014) **214**:2627–2636.

[10] Khairallah, S.A., Anderson, A.T., Rubenchik, A. and King, W.E. Laser powder-bed fusion additive manufacturing: Physics of complex melt flow and formation mechanisms of pores, spatter, and denudation zones. *Acta Materialia* (2016) **108**:36–45.

[11] Bierwisch, C., Kraft, T., Riedel, H. and Moseler, M. Three-dimensional discrete element models for the granular statics and dynamics of powders in cavity filling. *J. Mech. Phys. Solids* (2009) **57**:10–31.

[12] Bierwisch, C. A surface tension and wetting model for the δ^+-SPH scheme. In: *Proceedings of the 13th SPHERIC International Workshop 2018.* Quinlan, N.J., Tong, M., Moghimi, M.H. and McLoone, M. (Eds.). National University of Ireland, Galway, Ireland (2018) 95–102.

[13] http://www.simpartix.com